Printed-Board Inductive Loop Topologies Performance for Partial Discharges Detection

A. Imburgia, *Member, IEEE,* S. Kaziz, P. Romano, *Senior Member, IEEE,* D. Flandre, *Senior Member IEEE*, G. Artale, *Member, IEEE,* G. Rizzo, F. Viola, *Senior Member, IEEE*, G. Ala, *Senior Member, IEEE,* F. Tounsi

***Abstract*—Partial discharges (PD) are localized breakdowns in the insulation within high-voltage (HV) equipment and can be a warning sign of potential future failure. Regular PD monitoring through preventive maintenance is essential to the reliability of many expensive HV apparatuses. Hence, the purpose of this work is to assess the performance of a novel class of multi-turn inductive loop sensors based on printed circuit board (PCB) to detect PD in free space. Based on their topology, three distinct inductive sensors, named meander, non-spiral, and spiral, are evaluated towards detecting in-lab corona, internal, and surface PDs. Through simulations and measurements, the low-frequency lumped-element circuit model for each of the three magnetic field probes was extracted. Experimental PRPD patterns showed that the three evaluated inductive loops could be effectively applied for online monitoring and recognition of PDs. The experimental results show that the single PD pulses detected by the three sensors have a typical PD pulse shape that is a damped sinusoidal function with frequency spectra spanning from 14.84 MHz to 46 MHz. The spiral sensor yielded the maximum sensitivity, while the meander topology produced the lowest.**

***Index Terms*—PCB-based inductive loop, spiral inductor, partial discharge detection, PRPD patterns, magnetic-field measurement.**

I. INTRODUCTION

IN the field of medium- and high-voltage transmission systems, partial discharge (PD) phenomenon represents the main cause of insulator lifetime decline [1][2]. For this reason, over the years, several measurement techniques and detection schemes for PD have been developed [3]. Nowadays, PD monitoring is implemented in almost all electrical systems where the dielectric layer can be subjected to a high electric field gradient. These systems are not limited to medium- and high-voltage cables and their accessories but also include gas-insulated switchgear (GIS), generators, motors, transformers, power electronic devices, etc. [4][5]. Early diagnosis of PD is essential because it can prevent more significant damage to costly electrical apparatus [6][7]. When it comes to PD acquisition instruments, both wired and wireless tools exist on the market. Depending on the discharge source, the acquired PD pulses have different pattern s and frequency contents. Therefore, by means of dedicated software, it is possible to distinguish the type of PD (such as internal, surface, and corona discharge) and also separate the PD signal from the noise [8][9].

Various methods can be used to detect PD, such as electrical [10], chemical [11], acoustic (20 kHz to 1 MHz [12]), optical (300 GHz to 3000 THz [13]), and electromagnetic methods. During the past decades, several types of radiometric sensors have been developed, taking advantage of the electromagnetic waves produced during PD pulses [14]. All of these radiometric sensors, of different shapes, sizes, and operating principles, are designed to detect either the electromagnetic (EM) radiation emitted into the air or the PD pulse current flowing in the ground cable. The EM radiation emitted into the air consists of a combination of different frequency components up to a few GHz and falls within the range of the very high-frequency (VHF) and ultra-high-frequency (UHF) bands. Consequently, UHF and VHF antennas can detect these EM emissions and radio frequency interference associated with PD presence. On the other hand, once the EM wave hits the equipment chassis or the ground shield, it is transformed into a high-frequency current pulse in the 500 kHz to 100 MHz range, usually centered around 10 MHz, which can travel tens of meters along the ground cable [14]. This PD pulse waveform can generally be detected using an inductive loop sensor (ILS), a high-frequency current transformer (HFCT), or a Rogowski coil (RC), which are clamped around or placed close to the ground terminal of the HV equipment, allowing measurement of any emerging HF signals. Like HFCT and RC sensors, ILS are based on Faraday's law and measure the voltage induced in a loop through the change in the magnetic field caused by the PD pulse waveform. However, the use of these magnetic sensors is very limited since a short separation distance from the primary conductor must be respected, and they cannot provide information about PD localization, which restricts their use with real devices such as generators and transformers. In other ways, since EM waves in space consist of an electric field measured in V/m and a magnetic field measured in A/m, the

This paragraph of the first footnote will contain the date on which you submitted your paper for review, which is populated by IEEE. It is IEEE style to display support information, including sponsor and financial support acknowledgment, here and not in an acknowledgment section at the end of the article.

This work was supported in part by a Marie Skłodowska-Curie individual fellowship, project reference 101030887, and in part by the European Union-Fundo Social Europeu (FSE), PON Research and Innovation 2014-2020, project reference DM 1062/2021; *(Corresponding author: Fares Tounsi)*.

Antonino Imburgia, Pietro Romano, Giovanni Artale, Fabio Viola, and Guido Ala are with the Department of Engineering, University of Palermo, Palermo, Italy (e-mails: antonino.imburgia01@unipa.it; pietro.romano@unipa.it; giovanni.artale@unipa.it; fabio.viola@unipa.it; guido.ala@unipa.it).

Sinda Kaziz is with the Systems Integration and Emerging Energies (SI2E) Laboratory, National Engineering School of Sfax, University of Sfax, 3038 Sfax, Tunisia (e-mail: sinda.kaziz@fsm.u-monastir.tn).

Denis Flandre and Fares Tounsi are with the Institute for Information and Communication Technologies, Electronics, and Applied Mathematics (ICTEAM), Université catholique de Louvain, 1348 Louvain-la-Neuve, Belgium (e-mails: denis.flandre@uclouvain.be; fares.tounsi@uclouvain.be).

Giuseppe Rizzo is with Prysmian Group, 90128 Palermo, Italy. (e-mail: giuseppe.rizzo@prysmiangroup.com).

Color versions of one or more of the figures in this article are available online at http://ieeexplore.ieee.org

Digital Object Identifier

magnetic field perpendicular to the electric field can be detected separately. A loop antenna consisting of a wound conductive loop brought into resonance either with external capacitance or with built-in stray capacitance to form a high-Q parallel tuned circuit can be used [15]. However, the latter has a narrow frequency bandwidth and requires accurate tuning to ensure the antenna gain is maximized in the frequency band of interest.

Hence, in this article, we will test the capability of a new class of printed circuit board (PCB)-based multi-turn magnetic field sensors that does not operate at resonance, like the loop antenna, to detect PD in the air. Unlike the ILS, used to measure changes in the magnetic field surrounding the ground line, the new proposed sensor picks up the magnetic field from free space close to the equipment to be monitored according to Faraday's law of induction and could provide information about PD localization [16]. The main advantages of PCB technology lie in its low cost and small footprint. Therefore, this paper is a continuation of a previously published work that examined the suitability of two PCB-based inductive sensor topologies for in-lab PD detection [7]. Herein, another promising inductive sensor topology with a spiral multi-turn coil shape was constructed, evaluated, and compared to the other two as an extension of the previously carried out research.

This paper is organized as follows: Section II focuses on the design and fabrication of the inductive sensors and some theoretical background. FEM-based simulations using Ansys HFSS software and characterizations are presented in Section III, and Section V is devoted to the experimental setup. Lastly, a comparison of the detected PD signals, their frequency spectrum, and the acquired phase-resolved PD (PRPD) pattern obtained by the three sensors with those provided by the conventional measurement impedance is performed in Section VI.

II. Inductive Sensor Fabrication and Basis

With the aim of finding new low-cost and efficient solutions for PD monitoring, a PCB-based multi-turn inductive loop, referred to as a spiral inductor, was fabricated to evaluate its performance compared to two other sensors. In fact, in a previous investigation by the authors [7], two PCB-based sensors (referred to as meander and non-spiral) were proposed, studied, and assessed. The impedance moduli and phase angle, that yield the first self-resonant frequency (SRF) of the two sensors, were obtained using Ansys HFSS (high-frequency structure simulator). Furthermore, a 2D radiation pattern useful for determining the loop's sensitivity as a function of its orientation with respect to the PD source was also specified. We experimentally showed that for best sensitivity, as with dipole antennas, the inductive loop must be oriented at an angle of 90 degrees relative to the PD source (omnidirectional azimuth radiation pattern) [7]. Therefore, in the plane of the loop, the discharge magnitudes detected by the two investigated sensors were maximal and comparable. Additionally, experimental tests were conducted to assess the sensors' experimental performance in terms of corona PD detection. The tests involved a comparison of PD patterns, the single PD signal's shape, and their associated frequency spectrum. In addition, a comparison was made between the measurement outcomes from the two inductive sensors and a commercial high-frequency current transformer (HFCT) PD sensor. However, due to the differing environmental conditions, PD corona detection was reexamined in this paper for the meander and non-spiral sensors as well as for the spiral topology. Furthermore, surface and internal PD acquisitions were carried out for each of the three inductive loop sensors.

In this work, another type of PCB-based planar inductive loop was fabricated to assess its performance toward PD detection. The spiral inductor, whose layout is shown in Fig. 1a, is classified as a double-sided sensor, unlike the other two topologies, which are made on a single-layered substrate [7]. It consists of two metallization tracks, which are the spiral and the underpass, connected together during manufacture by means of two vias. The inductive loop is manufactured using the same process as the meander and non-spiral topologies on a double-layer PCB. That is, the spiral is drawn on the front side of a 17 µm-thick copper-cladded FR-4 board material, while the underpass is on the PCB bottom side. Table I lists the geometric dimensions of the sensor, where *n* is the number of turns. PCB-based sensors present several advantages over traditional ones, such as their compact size, inexpensive cost, and the fact that there is no need for an external power supply. Furthermore, it can be placed close to the PD source to increase its sensitivity.

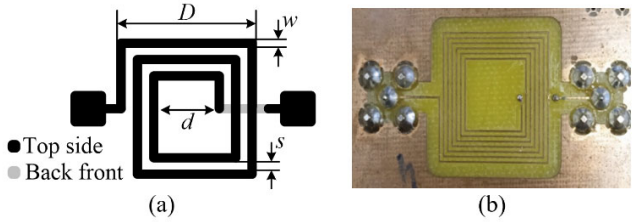

Fig. 1. The investigated multi-turn spiral inductive loop: (a) the layout (the number of turns is not compliant), and (b) the top side of the manufactured PCB-based loop.

Table I: Geometrical dimensions of the PCB-based spiral sensor.

Parameter	*n*	*D [mm]*	*d [mm]*	*w [mm]*	*s [mm]*
Value	6.5	20	10.4	0.4	0.4

The inductive, or induction, loop is one of the simplest, most versatile, and best-known types of magnetic field sensors. Their transfer function $\varepsilon = f(B)$ results from the fundamental Faraday's law of induction, where ε is the electromotive force and B is the magnetic field. Indeed, the temporal and/or spatial variations of the magnetic flux, Φ, through a conductive loop induce an electric vector field, which gives rise to an induced voltage defined as:

$$\varepsilon = -n\frac{d\Phi}{dt} = -n\,A\frac{dB}{dt} \quad (1)$$

where A is the area of the coil and n is the number of turns. It is known that inductive loops are often used as electromagnetic field probes in the microwave bands (up to ~3 GHz). In fact, the electromotive force induced in the receiving multi-turn inductive loop is precisely proportional to the rate of change of magnetic flux in surrounding free space over time across the loop surface. The latter is equivalent to n times the average side of the spiral inductor. At the frequencies of interest (i.e., << SRF), the gain is 0 dB and the output voltage is directly the induced voltage in the loop [17].

III. THE MULTI-TURN SPIRAL LOOP CHARACTERISTICS

The spiral sensor was simulated using Ansys HFSS, and Fig. 2 illustrates the impedance modulus and the phase curves versus frequency. As shown in Fig. 2, the impedance initially rises almost linearly with frequency, exhibiting inductive behavior up to the loop's SRF, estimated roughly at 100 MHz. The spiral inductor will act inductively below this frequency and capacitively above it due to the effect of self-capacitance, which lowers the equivalent impedance. At frequencies much below 100 MHz, the phase angle is 90 degrees, and the inductive sensor could function as a magnetic loop receiver. Starting from the impedance modulus and the phase, the lumped-element electrical parameters were extracted. Fig. 3 displays the low-frequency lumped-element circuit model of the designed multi-turn inductive loop. The latter is composed of an inductor L_s representing the self-inductance of the traces in series with a resistor R_s (including frequency related losses), both of which are parallel to an inter-strip stray capacitor C_s, which is mainly a function of the number of turns and the inter-turn distance. The voltage generator refers to the electromotive voltage generated by the spiral (see Eq. 1) upon variation of the magnetic field. It is worth mentioning that, below the SRF, the circuit parameters of the equivalent electrical model may be assumed to be constant (invariant with frequency). The SRF can be accurately calculated according to the electrical parameters of the inductor as:

$$SRF = \frac{1}{2\pi}\sqrt{\frac{1}{L_s\,C_s} - \frac{R_s^2}{L_s^2}} \qquad (2)$$

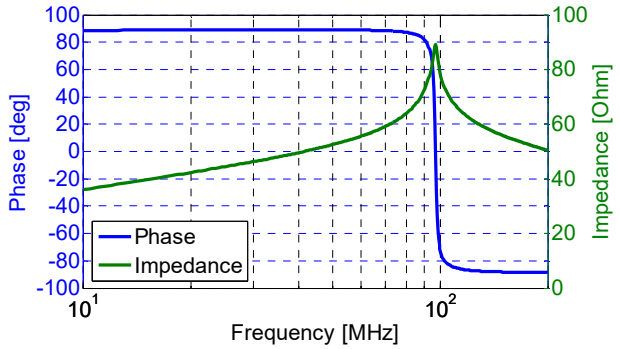

Fig. 2. Simulated impedance module and phase angle of the inductive planar spiral inductive loop.

It must be pointed out that the inductive loop is operational only in the bandwidth where the circuit is inductive, i.e., between the frequencies $R_s/2\pi L_s$ (~160 kHz) and the SRF. Obviously, the more the operating frequency increases, the more the ohmic losses increase due to skin and proximity effects. The different inductive loop lumped elements were also extracted with measurements using a vector network analyzer (Keysight E5061B ENA, 100 kHz to 3 GHz). Table II exhibits the various parameters extracted from simulations and measurements for all three inductive loop topologies. The measured values agree fairly well with the simulated ones. The difference may be partly due to a 5% error in the width of the tracks during the milling process but will not impact the present PD detection analysis. As seen, the spiral inductive loop shows the highest inductance value, which is due to the high mutual inductance generated between its parallel segments. Moreover, it has the highest values of C_s, which have a substantial effect on reducing its resonant frequency. Of the three inductors, the non-spiral has the highest resonance frequency, which is due to its lowest resistance value. Lastly, compared to the spiral inductor, the meander exhibits higher SRF and lower self-inductance values, which is due to the antiparallel current flow segments forming the inductor.

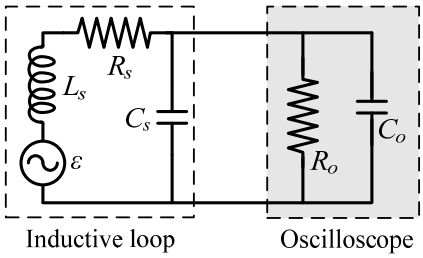

Fig. 3. The lumped-element circuit model of the inductive loop (for frequencies below its SRF) [18].

Table II: Values of simulated/measured electrical parameters of the various inductive loop.

Parameters/Topology		Spiral	Meander	Non-Spiral
L_s (@1 MHz) [nH]	Simu	997	190	19
	Meas	1000	185	22
R_s (@1 MHz) [Ω]	Simu	1.03	0.99	0.04
	Meas	0.95	1.3	0.06
C_s [pF]	Simu	2.53	0.59	1.1
	Meas	2.5	0.62	1.06
SRF [MHz]	Simu	99	608	1100
	Meas	130	463	1085
Q_{max}	Simu	75 @34 MHz	52 @211 MHz	125 @161 MHz

The performance of an inductor is mainly determined by its quality factor, Q, which affects the circuits and/or devices in which it is implemented. The quality factor of an inductor is defined as $2\pi f$ times the ratio between the peaks of stored magnetic energy E_{stored} and the dissipated/lost energy E_{lost} over one oscillation cycle, as [19]:

$$Q = 2\pi\frac{E_{stored}}{E_{lost}} = -\frac{\omega\,(C_s R_s^2 - L_s + C_s L_s^2\omega^2)}{R_s} \qquad (3)$$

The given Q-factor expression, which is frequency-dependent, should take into account the parasitic capacitance and skin and proximity effects on the metallic layer's resistance. Fig. 4 shows the simulated quality factor of the three topologies. A greater Q-factor indicates a lower rate of energy loss and a slower decay of oscillations. As shown, the spiral shows a maximum quality factor Q_{max} of 75 at 34 MHz and an SRF of ~100 MHz, while the meander presents the lowest quality factor of 52 at ~210 MHz and has an SRF of about 600 MHz. The quality factor of the non-spiral increases up to 125 at 161 MHz.

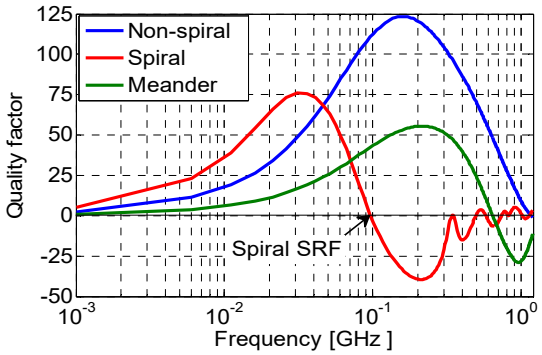

Fig. 4. The simulated quality factor of the three assessed inductive sensor topologies.

IV. Experimental Setup

In order to experimentally compare and validate the three PCB-based inductive loops in terms of their ability to detect PD, a series of experimental tests were carried out. As a tool for result comparison, the conventional measurement method using a coupling capacitor and measurement impedance of 50 Ω (quadripole) was chosen [20]. Hence, the output PD pulse magnitude is more or less a measure of the PD current amplitude, which reflects the PD severity. The measurement configuration adopted is reported in Fig. 5. In this case, the arranged measurement setup complies with the IEC 60270 standard, and therefore the coupling capacitor has been connected in series with the measurement impedance. The setup is made up of a high-voltage AC generator, the coupling capacitor, copper pipes for electrical connections, the PD sensor represented by the inductive loop, the 50 Ω measurement impedance, the PryCam grids, and the PD source [21]. For the latter, three different specimens capable of generating internal, surface, and corona PDs were used. The PryCam Grids consist of remotely activatable input channels that receive as input data, separately and not simultaneously, the PD signals detected by the sensor and by the 50 Ω measurement impedance. The output of the PryCam Grids is sent in real-time to a computer and thus to acquisition and processing software, where the phase-resolved PD (PRPD) pattern, the single PD pulse, and the frequency spectrum are displayed. For acquisition with the PCB-based loop, the PD signals are picked up electromagnetically and sent directly to the PryCam grids without involving the coupling capacitor. For acquisitions made through the measurement impedance, the detected PD signals flow through the ground.

In the measurement setup, the PCB-based inductive loop was located 9 cm away from the PD source. Furthermore, the 2D radiation pattern described in [7] suggests that the optimal signal sensitivity is achieved when the inductive loop is oriented at a 90° angle with respect to the PD source, as illustrated in Fig. 6. Noteworthy the sensor output is directly connected to the PryCam grids, which has an internal amplifier of 40 dB. The configurations used for the three specimens generating internal, surface, and corona PD phenomena are reported in Fig. 7. To lower the partial discharge inception voltage (PDIV) for internal discharges, the air void was brought into contact with the upper HV electrode. For all three PD source specimens, the PDIV detected is the same and equal to 3 kV.

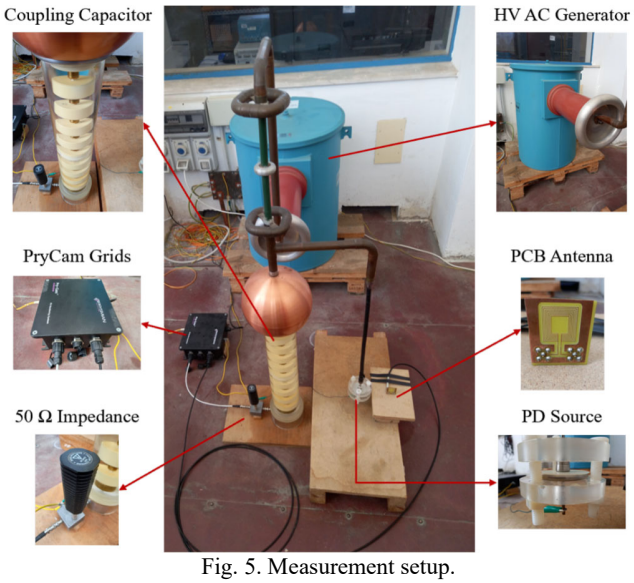

Fig. 5. Measurement setup.

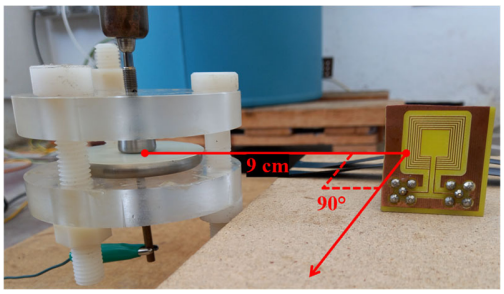

Fig. 6. The PCB-based antenna sensor positioned at a distance of 9 cm and at an angle of 90° from the surface PD source (azimuthal directivity).

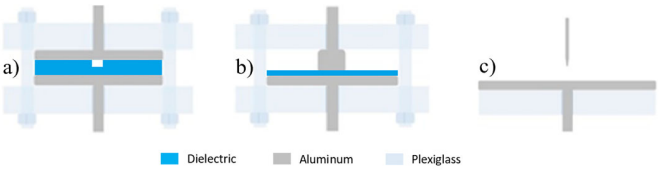

Fig. 7. Configurations of the PD sources generating: (a) internal, (b) surface, and (c) corona PDs.

V. Measurement Results

The PD detections with the three inductive loop sensors were performed under the same measurement conditions. For a complete characterization of the PRPD pattern, a single acquired PD pulse and its frequency spectrum detected by each inductive loop are reported and analyzed. In addition, the measurement results provided by each topology were compared with those obtained using the measurement impedance.

A. Internal PD measurement

The PRPD patterns acquired from the three topologies as well as from the measurement impedance are depicted in Fig. 8. The PRPD plot shows the amplitude of each discharge event (*y*-axis) plotted against its phase angle (*x*-axis). In this figure, the PD amplitude is measured in mV using the loop sensor, and a fixed duration of 30 seconds of activity is displayed against the system frequency of 50 Hz. Each PRPD

pattern will be unique, as each discharge fault will be slightly different from each other as the physical fault will be of a certain type and form. It is noteworthy to highlight that the patterns detected by the three different kinds of loop sensors qualitatively matches the pattern detected by the measurement impedance, demonstrating their capacity to identify and discriminate between different kinds of defects via the PRPD.

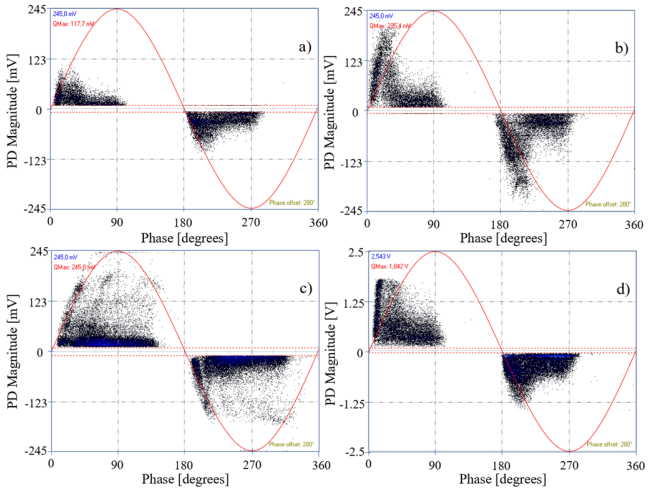

Fig. 8. PRPD pattern for internal PD obtained from the: (a) meander inductive loop, (b) non-spiral inductive loop, (c) spiral inductive loop, and (d) measurement impedance.

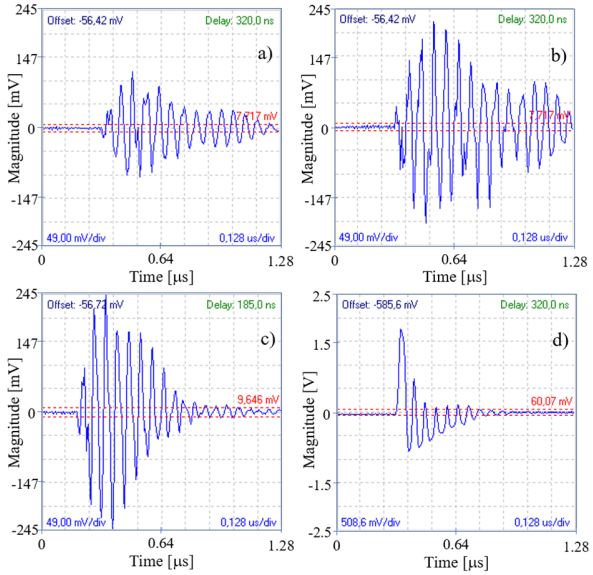

Fig. 9. Single PD pulse for internal PD detection by the: (a) meander inductive loop, (b) non-spiral inductive loop, (c) spiral inductive loop, and (d) measurement impedance.

The single PD pulse waveform and its associated frequency spectrum detected from the acquisition system of the tested devices are reported in Fig. 9 and Fig. 10, respectively. The recorded data show that all PD signals have the damped sinusoidal function that characterizes a typical PD pulse shape. As can be observed, the maximum magnitude of the PD pulse is detected by the spiral, resulting in V_{MAX} = 245 mV. Consequently, the highest sensitivity for internal PD detection is associated with the spiral topology. On the other hand, the non-spiral and meander topologies exhibit sensitivity with V_{MAX} values equal to 235.47 mV and 117.7 mV, respectively. However, the three PD single signals have nearly identical frequency contents, though, with a peak value between 14.84 MHz and 16.41 MHz. Compared to the acquisition provided by the measurement impedance, the most significant difference can be observed in the greater amplitude and less oscillating shape of the detected PD pulse (Fig. 9). In spite of this, the frequency spectrum peak (Fig. 10) and the shape and phase angle of the PRPD pattern (Fig. *8*) are comparable to those derived from the three inductive loops.

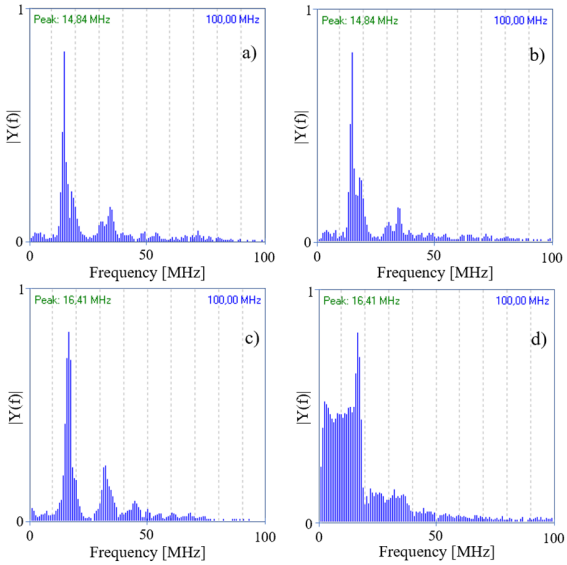

Fig. 10. Frequency spectrum of the detected internal PD pulse acquired by the: (a) meander inductive loop, (b) non-spiral inductive loop, (c) spiral inductive loop, and (d) measurement impedance.

B. Surface PD measurement

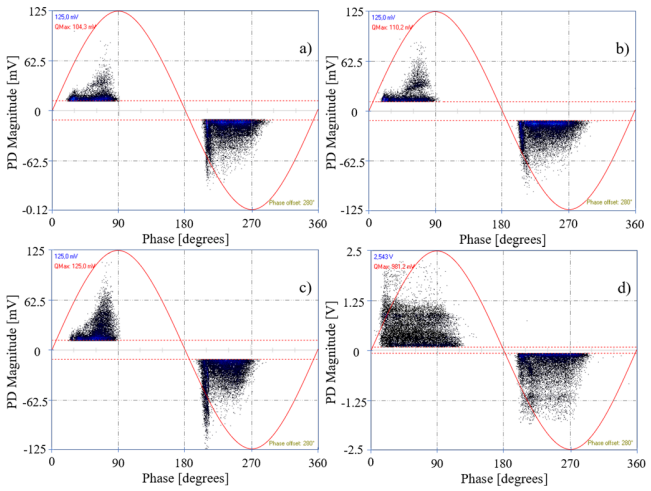

Fig. 11. PRPD pattern for surface PD acquired by the: (a) meander inductive loop, (b) non-spiral inductive loop, (c) spiral inductive loop, and (d) measurement impedance.

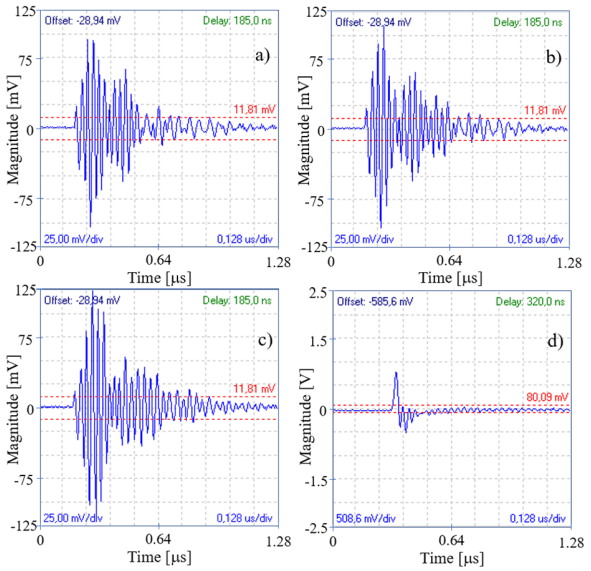

Fig. 12. Single PD pulse for surface PD acquired by the: (a) meander inductive loop, (b) non-spiral inductive loop, (c) spiral inductive loop, and (d) measurement impedance.

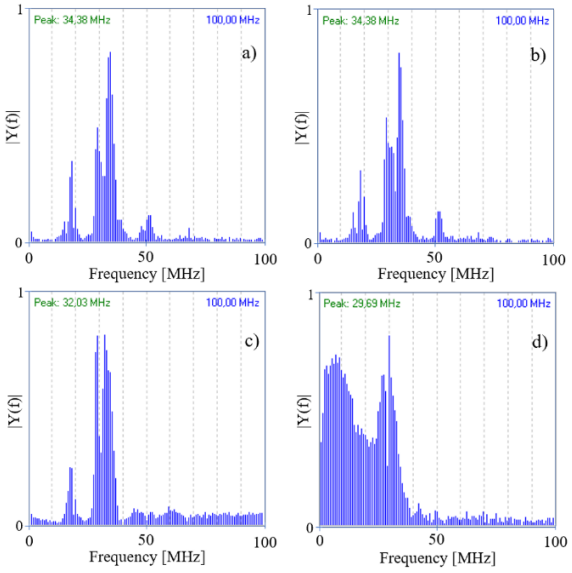

Fig. 13. Frequency spectrum of the detection of surface PD acquired by the: (a) meander inductive loop, (b) non-spiral inductive loop, (c) spiral inductive loop, and (d) measurement impedance.

Regarding surface PD detections, the obtained PRPD patterns, acquired single PD pulses, and frequency spectrum are illustrated in Fig. 11, Fig. 12, and Fig. 13, respectively, for each of the four sensors. By comparing the PRPD patterns of all inductive loops, the higher PD magnitude detected can again be attributed to the spiral inductive loop. On the other hand, as can be seen in Fig. 11c, when the PRPR patterns obtained from the three PCB-based inductive loops are compared with those of the measurement impedance, it turns out that all the tested topologies could effectively be applied for online monitoring and recognition of surface PD. However, the measurement impedance is capable of detecting a higher number of PD events with greater magnitude. The analysis of the single PD pulses acquired by the inductive loops reveals a strong oscillation compared to that associated with the measurement impedance, which exhibits a more standard shape (Fig. 12), which could be easily filtered by a suitable circuit. The frequency content of the detected PD signals exhibits a similar frequency peak across the four measured sensors, falling within the range of 32.03–34.38 MHz. Nevertheless, the signal detected by the measurement impedance has a large low-frequency content in addition to a frequency peak at around 29.7 MHz.

C. Corona PD measurement

Previous work has only used the needle-plane specimen configuration for corona discharge generation [7]. In the current work, the corona PD measurements were repeated for the three sensors and the 50 Ohm impedance in order to provide a reliable comparison that takes the environmental conditions into consideration. The obtained PRPD is reported in Fig. 14, showing that all three loop topologies could be effectively applied for online monitoring and recognition of Corona PD. In this pattern, the meander inductive loop shows lower-magnitude PD signals, while the spiral antenna continues to detect the highest-magnitude signals. However, as in the previous two tests, the measurement impedance shows that the amplitude of the detected signals is an order of magnitude higher than that of the three PCB-based loops, as can be observed in Fig. 14c. Regarding the shape of the single PD pulses detected by the inductive loops (Fig. 15a–c), a strong oscillation can be observed. Rather, as depicted in Fig. 15d, a more defined pulse shape is provided by the measurement impedance. The frequency spectrum corresponding to the PD pulses in Fig. 15 is reported in Fig. 16. The analysis of these graphs reveals that although the frequency content of the signal detected by the measurement impedance is very different, the three inductive loops exhibit similar behavior. In fact, the latter provides a 2.34 MHz frequency spectrum peak, whereas the peaks associated with the three inductive loops fall within the 34.38–46.09 MHz range.

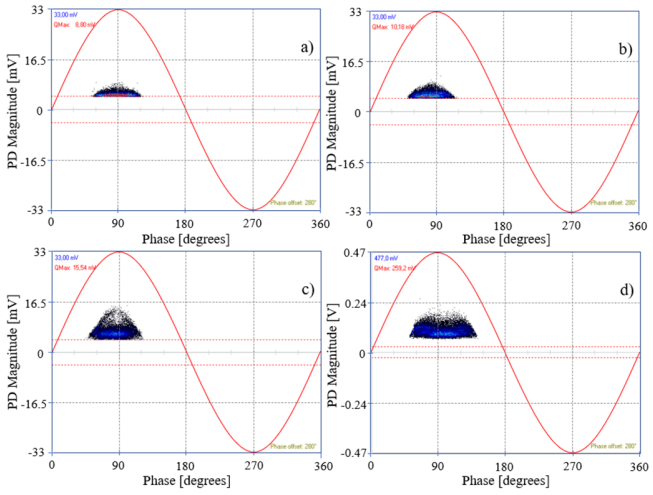

Fig. 14. PRPD pattern for corona PD obtained from the: (a) meander inductive loop, (b) non-spiral inductive loop, (c) spiral inductive loop, and (d) measurement impedance.

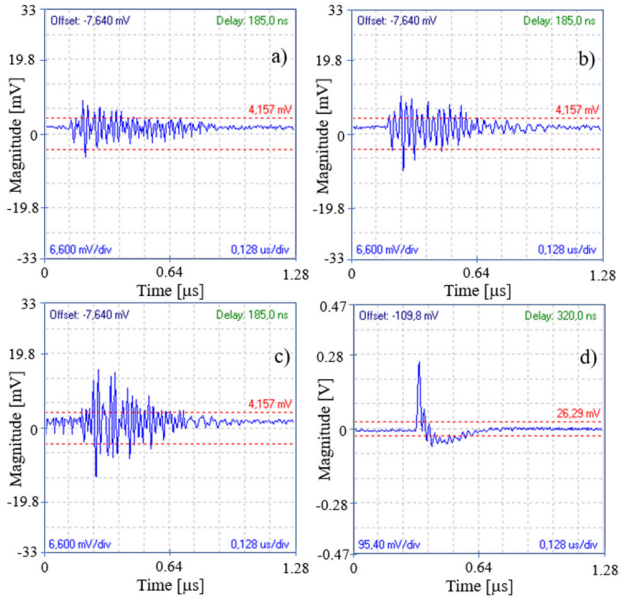

Fig. 15. Single PD pulse for corona PD detection by the: (a) meander inductive loop, (b) non-spiral inductive loop, (c) spiral inductive loop, and (d) measurement impedance.

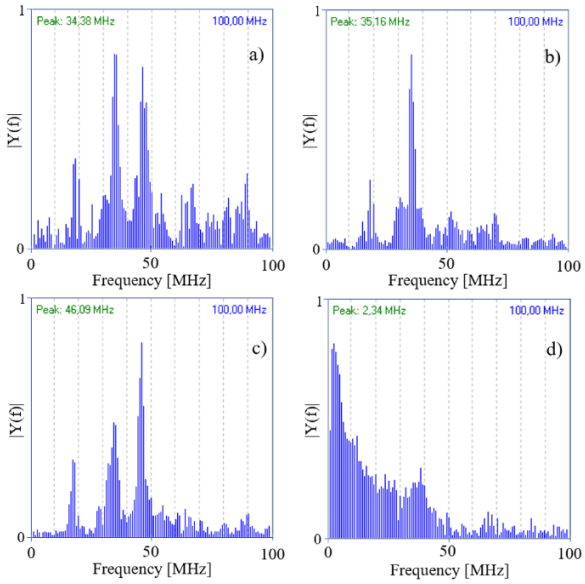

Fig. 16. Frequency spectrum of the detected corona PD pulse acquired by the: (a) meander inductive loop, (b) non-spiral inductive loop, (c) spiral inductive loop, and (d) measurement impedance.

VI. Summary and Discussion

For all PD sensors tested, the maximum detected PD signal magnitudes are summarized in Table III for the three different PD sources. The spiral inductive sensor, as highlighted, has the highest sensitivity for the acquisition of internal, surface, and corona discharges. This is due to the fact that the latter has the highest self-inductance value when compared to the non-spiral and meander topologies and has an appropriate wrapped shape. Most importantly, it has a higher quality factor profile in the frequency range of 1 to 47 MHz. The meander, on the other hand, provided the lowest PD signal sensitivity, which may be justified by the fact that its quality factor distribution in the frequency range of interest is lower. Finally, an intermediate behavior is attributed to the non-spiral. In fact, the performance of an inductor is mainly determined by its quality factor, which affects the circuits and/or devices in which it is implemented. A higher Q indicates a lower rate of energy loss relative to the stored energy of the resonator; the oscillations die out more slowly. Furthermore, from Table III, a comparison of the PD amplitude values detected by the impedance measurement with those detected by the three inductive loops highlights that the latter can provide detectable and proportional values to discharge severity. With primary attention to describing the performance tradeoffs of small-size, the proposed inductive loops perform well. Moreover, we must also emphasize the difficulties associated with the conventional method, which entails carrying and then halting the HV apparatus to the laboratory in order to connect the coupling devices. It can also be seen that, for internal discharge, the three topologies showed a spectrum frequency content in the range of 14.84–16.41 MHz, while it was in the range of 32.03–34.38 MHz for surface PD and 34.38–46.09 MHz for corona PD. These spectra are, in fact, lower than the highest frequency of consideration in the spectrum of the partial discharge signal to avoid oscillations. In addition, these frequency spectra show a narrow bandwidth and are very similar to those recorded by the measurement impedance, which has the drawback of high low frequency content.

Table III. Summary of the maximum amplitude of PD signals detected from the three PD sources.

Antenna/Defects	Meander	Non-Spiral	Spiral	Impedance
Internal PD (mV)	117.7	235.4	245	1842
Surface PD (mV)	104.3	110.2	125	981.2
Corona PD (mV)	8.8	10.18	15.54	259.2

VII. Conclusion

In this work, the capability of meander, non-spiral, and spiral inductive loop sensors was investigated from the perspective of PD detection. The operating principle of these loop probes is based on Faraday's law of electromagnetic induction. Simulations were carried out in order to extract their frequency behavior. Through simulations and measurements, the low-frequency lumped elements circuit model for each of the three magnetic field probes was extracted. This model is accurate, under certain assumptions, but breaks down as the inductor approaches resonance, which does not impact the PD detection results discussed in this paper. The three sensors were experimentally tested for PD detection. The PD phenomena have been generated using artificial specimens for corona, surface, and internal discharge. Experimental results show that for the three PD sources, the spiral inductive loop has the highest sensitivity. The experimental PRPD patterns showed that the three evaluated inductive loops could be effectively applied for online monitoring and recognition of PDs. Finally, the performance of the three sensors was compared to the conventional measurement impedance, which exhibited higher sensitivity but similar PRPD patterns. In future work, integrated

inductive loops could be assessed in order to be inserted into apparatus where available space is limited.

REFERENCES

[1] J.M. Rodríguez-Serna, R. Albarracín-Sánchez, "A Study on the Life Estimation and Cavity Surface Degradation Due to Partial Discharges in Spherical Cavities within Solid Polymeric Dielectrics Using a Simulation Based Approach". *Polymers* 2021, *13*, 324.

[2] Morshuis, P.H. "Degradation of solid dielectrics due to internal partial discharge: Some thoughts on progress made and where to go now". *IEEE Trans. Dielectr. Electr. Insul.* 2005, 12, 905–913.

[3] P. Romano, A. Imburgia, G. Ala, "Partial Discharge Detection Using a Spherical Electromagnetic Sensor". *Sensors* 2019, *19*, 1014.

[4] M. R. Hussain, S. S. Refaat and H. Abu-Rub, "Overview and Partial Discharge Analysis of Power Transformers: A Literature Review," in IEEE Access, vol. 9, pp. 64587-64605, 2021.

[5] N. Rosle, N. A. Muhamad, M. N. K. H. Rohani and M. K. M. Jamil, "Partial Discharges Classification Methods in XLPE Cable: A Review," in IEEE Access, vol. 9, pp. 133258-133273, 2021.

[6] L. A. Renforth, R. Giussani, M. T. Mendiola, and L. Dodd, "Online partial discharge insulation condition monitoring of complete high-voltage networks," *IEEE Transactions on Industry Applications*, vol. 55, no. 1, pp. 1021–1029, 2018.

[7] A. Imburgia, S. Kaziz, P.Romano, D. Flandre, G. Artale, G. Rizzo, F. Viola, F. Tounsi, G. Ala, "Investigation of PCB-based Inductive Sensors Orientation for Corona Partial Discharge Detection," 2022 IEEE 21st Mediterranean Electrotechnical Conference (MELECON), Palermo, Italy, 2022, pp. 559-563.

[8] H. Ma, J. C. Chan, T. K. Saha and C. Ekanayake, "Pattern recognition techniques and their applications for automatic classification of artificial partial discharge sources," in IEEE Transactions on Dielectrics and Electrical Insulation, vol. 20, no. 2, pp. 468-478, April 2013.

[9] A. Contin and S. Pastore, "Classification and separation of partial discharge signals by means of their auto-correlation function evaluation," in IEEE Transactions on Dielectrics and Electrical Insulation, vol. 16, no. 6, pp. 1609-1622, December 2009.

[10] Ali Reza Abbasi, "Fault detection and diagnosis in power transformers: a comprehensive review and classification of publications and methods", in Electric Power Systems Research, Volume 209, 2022.

[11] H. Khelifa, E. Vagnon and A. Beroual, "AC Breakdown Voltage and Partial Discharge Activity in Synthetic Ester-Based Fullerene and Graphene Nanofluids," in IEEE Access, vol. 10, pp. 5620-5634, 2022.

[12] Viral B. Rathod, Ganesh B. Kumbhar & Bhavesh R. Bhalja, "Partial Discharge Detection and Localization in Power Transformers based on Acoustic Emission: Theory, Methods, and Recent Trends", IETE Technical Review, Vol. 39, no. 3, pp. 540-552, 2021.

[13] C. Xia, M. Ren, R. Chen, J. Yu, C. Li, Y. Chen, K. Wang, S. Wang, M. Dong, "Multispectral Optical Partial Discharge Detection, Recognition, and Assessment," in IEEE Transactions on Instrumentation and Measurement, vol. 71, pp. 1-11, 2022.

[14] S. Kaziz, M.H. Said, A. Imburgia, B. Maamer, D. Flandre, P. Romano, F. Tounsi, "Radiometric Partial Discharge Detection: A Review". *Energies* 2023, *16*, 1978.

[15] N. Zeidi, S. Kaziz, M. H. Said, L. Rufer, A. Cavallini, and F. Tounsi, "Partial discharge detection with on-chip spiral inductor as a loop antenna," *Review of Scientific Instruments*, vol. 92, no. 9, p. 094701, 2021.

[16] Kaziz, S.; Romano, P.; Imburgia, A.; Ala, G.; Sghaier, H.; Flandre, D.; Tounsi, F. PCB-Based Planar Inductive Loops for Partial Discharges Detection in Power Cables. *Sensors* 2023, *23*, 290.

[17] G. Robles; J.M. Martínez; M. Rojas; and J. Sanz, "*Inductively coupled probe for the measurement of partial discharges*," Rev. Sci. Instrum, Vol. 79, p. 055104, 2008.

[18] D. C. Yates, A. S. Holmes, and A. J. Burdett, "Optimal transmission frequency for ultralow-power short-range radio links," *IEEE Transactions on Circuits and Systems I: Regular Papers*, vol. 51, no. 7, pp. 1405–1413, 2004.

[19] O. Kenneth, "Estimation methods for quality factors of inductors fabricated in silicon integrated circuit process technologies," IEEE Journal of Solid-State Circuits, vol. 33, no. 8, pp. 1249-1252, Aug. 1998.

[20] D. A. do Nascimento, Y. Iano, H. J. Loschi, L. A. de Sousa Ferreira, J. A. D. Rossi, and C. D. Pessoa, "Evaluation of Partial Discharge Signatures Using Inductive Coupling at On-Site Measuring for Instrument Transformers" International Journal of Emerging Electric Power Systems, vol. 19, no. 1, 2018.

[21] A. A. Jaber, P. I. Lazaridis, M. Moradzadeh, I. A. Glover, Z. D. Zaharis, M. F. Q. Vieira, M. D. Judd, R. C. Atkinson, "Calibration of free-space radiometric partial discharge measurements," in *IEEE Transactions on Dielectrics and Electrical Insulation*, vol. 24, no. 5, pp. 3004-3014, Oct. 2017.